

Comparison of computational and experimental results for a transonic variable-speed power-turbine blade operating with low inlet turbulence levels

David T. Booth¹

U.S. Army Research Laboratory, Aberdeen Proving Ground, Maryland 21005

Ashlie B. Flegel²

NASA Glenn Research Center, Cleveland, Ohio, 44135

A computational assessment of the aerodynamic performance of the midspan section of a variable-speed power-turbine blade is described. The computation comprises a periodic single blade that represents the 2-D Midspan section VSPT blade that was tested in the NASA Glenn Research Center Transonic Turbine Blade Cascade Facility. A commercial, off-the-shelf (COTS) software package, Pointwise and CFD++, was used for the grid generation and RANS and URANS computations. The CFD code, which offers flexibility in terms of turbulence and transition modeling options, was assessed in terms of blade loading, loss, and turning against test data from the transonic tunnel. Simulations were assessed at positive and negative incidence angles that represent the turbine cruise and take-off design conditions. The results indicate that the secondary flow induced at the positive incidence cruise condition results in a highly loaded case and transitional flow on the blade is observed. The negative incidence take-off condition is unloaded and the flow is very two-dimensional. The computational results demonstrate the predictive capability of the gridding technique and COTS software for a linear transonic turbine blade cascade with large incidence angle variation.

Nomenclature

C_f	= skin friction coefficient, $C_f = \tau_{wall} / \frac{1}{2} \rho U^2$
C_{p_s}	= static pressure coefficient, $C_{p_s} = (P - P_2) / (P_{t,1} - P_2)$
C_{p_t}	= total pressure coefficient, $C_{p_t} = (P_{t,1} - P_t) / (P_{t,1} - P_2)$
C_x	= blade axial chord
H	= blade span
i	= incidence angle (deg.), $i = \beta_1$ – inlet metal angle (34.2 °)
M	= Mach number
PR	= pressure ratio, $PR = P_{t,1} / P_2$
P	= static pressure
P_t	= total pressure
Re	= Reynolds number, $Re = \rho U C_x / \mu$
S	= blade pitch
Tu	= turbulence intensity, $Tu = \text{SQRT}(\text{ave } u'^2_s + \text{ave } u'^2_z) / U$
u'	= fluctuating component of velocity
U	= free stream velocity
x	= axial coordinate
y	= pitchwise coordinate

¹ Research Aerospace Engineer, Army Research Laboratory, Aberdeen Proving Ground, 4603 Flare Loop, Aberdeen, MD, 21005, AIAA Member.

² Aerospace Research Engineer, Turbomachinery and Heat Transfer Branch, 21000 Brookpark Rd., Mail Stop 5-11, AIAA Member.

z	= spanwise coordinate
β_1	= relative inlet flow angle (deg.), $\beta_1 = \tan^{-1}(U_y / U_x)$
δ	= boundary layer thickness
μ	= dynamic viscosity
ρ	= density
τ_{wall}	= wall shear stress

Subscripts

1	= based on inlet condition
2	= based on exit condition
i	= isentropic value
s	= streamwise component
t	= total condition

I. Introduction

THE present study is part of an effort underway at the Army Research Laboratory (ARL) to develop modeling and simulation capabilities of turbine blade aerodynamics. The goal of this effort is to develop a robust and efficient process for analysis of proposed turbine blade designs that have increased performance. The use of Computational Fluid Dynamics (CFD) has the potential to aid in the design process of new blade types by reducing the time and cost associated with experimental testing. Evaluation of a commercial off the shelf (COTS) software was performed using a 3-D model of a candidate Variable-Speed Power-Turbine (VSPT) blade tip section of a notional large civil tilt rotor vehicle.

Power-turbine blades of conventional rotorcraft turboshaft engines are optimized to operate at nearly a fixed speed and a fixed incidence angle. The VSPT is a potential enabling technology for high speed tilt rotorcraft, where the power-turbine speed is slowed down by as much as 51% during cruise flight compared to take-off (hover) flight¹. Significant design challenges exist for the VSPT, due to this speed change, such as high work factors at cruise, large incidence angle variation (40° to 60°), and low aft stage Reynolds numbers at 28 kft cruise flight². The experimental results indicate the design/cruise condition of the VSPT blade is highly loaded with transitional flow, while the take-off condition represents an extreme off-design operating condition where the blade row is unloaded and the flow is very two-dimensional across the blade surface. Due to the empirical nature of turbulence modeling in CFD, this case is a challenging condition to accurately model and therefore is strongly suited for this code assessment effort.

VSPT research was conducted by NASA Glenn Research Center (GRC) and ARL as a potential solution for maintaining turbine blade aerodynamic performance for variable-speed power-turbines³. Experiments were performed on a candidate VSPT blade mid-span section in the Transonic Turbine Blade Cascade Facility at NASA GRC⁴. The experimental data of Flegel-McVetta *et al.*, 2013⁴ were acquired at low inlet turbulence intensity, over a range of Reynolds numbers, at engine/mission-relevant exit Mach numbers, and over a wide range of incidence angles, +15.8° to -51.0°. The inlet flow of the experiment was well characterized in terms of inlet boundary-layer thickness, inlet turbulence intensity, and dissipation/length-scale using two-point hotwire measurements. Because the Reynolds numbers of the tunnel were higher than in VSPT application, Flegel-McVetta *et al.*, 2013⁴ chose to test without an inlet turbulence grid so that the flow would be transitional, mimicking low Reynolds operation at engine relevant turbulence intensities.

CFD computations were obtained at the turbine cruise design point condition corresponding to an inflow angle of 40° and a take-off design point condition of the blade corresponding to an inflow angle of -2.5°. The computations were compared to measured blade loading, midspan loss, and turning provided by Flegel-McVetta *et al.*, 2013⁴. Steady state and time accurate Reynolds-averaged Navier-Stokes (RANS) computations were performed on a structured grid at the two design point conditions of the VSPT blade. Taking advantage of the periodicity of the blades in the cascade facility, the computational domain of the grid includes a single blade with periodic boundary conditions in the pitchwise directions as a representation of a periodic linear cascade.

II. Computational Approach

This section contains the description of the computational approach used in the study. The first subsection highlights salient features of the flow solver, the second subsection describes the CFD mesh and mesh generation process, and the third subsection presents the computational parameters of the simulations.

A. Flow Solver

3-D steady-state (RANS) and time-resolved (URANS) computations were conducted. A COTS code was used with a multi-block structured grid. For this study CFD++ version 14.1 was the chosen COTS⁵. Computations were run in parallel on a Department of Defense Supercomputing Resource Center (DRCE) supercomputer. The selected equation set was a pressure-based compressible perfect gas Navier-Stokes solver. The spatial discretization used by the code is a multi-dimensional Total Variation Diminishing (TVD) polynomial interpolation determined through limited reconstructions over cells and/or nodes. Spatial discretization was second order with node based polynomials. The local Courant number was used to accelerate convergence and second order dual time stepping technique was selected for time accurate computations.

Several turbulence and transition models are included in the CFD++ code, including the two-equation realizable k-epsilon model, two-equation R-gamma model, two-equation Shear Stress Transport (SST) model, and four-equation Langtry-Menter model. An algebraic transition prediction model, “Algebraic I”, can be used in conjunction with the realizable k-epsilon turbulence model that is based on modifying the generation term, applied to both k- and epsilon- transport equations⁶. A second algebraic transition model, “Algebraic II”, can be used with the SST turbulence model. The R-gamma and Langtry-Menter models are both transition prediction models.

Prior comparisons of the code in predicting transition were performed by Metacomp Technologies, Inc. using the above models with flat plate, Aerospatiale A airfoil, and S809 airfoil examples. The flat plate examples were tested at two different Tu_1 and the R-gamma model yielded the overall best prediction in terms of transition location. The k-epsilon and Algebraic I model and the Langtry-Menter model had the best agreement with the data for the airfoil examples⁶.

As these studies showed the k-epsilon and Algebraic I model and the Langtry-Menter model had best agreement with the data for the airfoil examples, and these models can be used in conjunction with the Musker inlet velocity profile boundary condition, described later in this paper, these models were chosen for use in this study. For comparative purposes, the SST and Algebraic II model were also compared to the measurements.

B. CFD Mesh

A 3-D structured mesh was generated from the experimental blade coordinate data using Pointwise version 17.0.1⁷ as depicted in Fig. 1. The mesh models the flow passage around a single blade with the suction and pressure surfaces located on the upper and lower surfaces, respectively. There is no blade tip gap and a viscous no-slip wall boundary condition was used for the endwall boundary. Due to symmetry in the spanwise direction, one half of the blade span was modeled with a symmetric boundary condition at the half span location. Periodic boundary conditions were used for the upper and lower boundaries of the grid, which are located approximately $0.5S$ above and below in the pitchwise direction of the blade surfaces. The inlet boundary condition is located at approximately $0.415C_x$ upstream of the blade leading edge to correspond to the experimental inlet measurement station. The exit boundary condition is approximately $1.0C_x$ downstream of the trailing edge to correctly capture the wake region. A back pressure imposition boundary condition was placed there to match the measured exit pressure. The grid was rotated about the center of the blade in the z-direction in order to change the incidence of the blade with respect to the incoming flow, which is fixed in the x-direction.

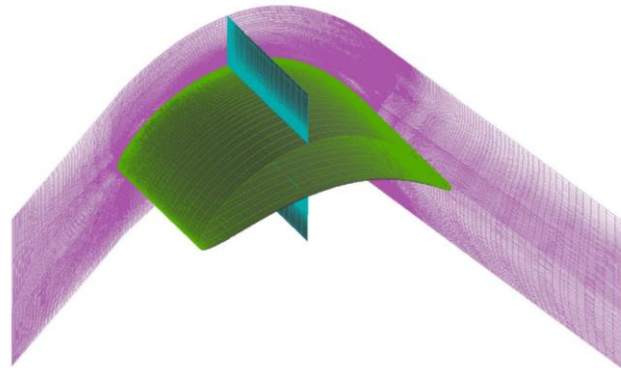


Figure 1. Three-dimensional grid of VSPT blade.

A Musker inlet velocity profile boundary condition was used for the inlet boundary to correctly specify the spatial variation in both turbulence energy and length scale and match the experimental inlet conditions. This boundary condition provided by the CFD++ code for internal flow parallel to one or more solid walls allows the user to prescribe a fully-developed turbulent boundary-layer profile for all mean-flow and turbulence-related quantities. The generated boundary-layer profile is based on Musker’s 1979 formulation⁶ in conjunction with a compressibility transformation and temperature fit due to Van Driest.⁶ Turbulence quantities in the boundary layer are determined as a functions of the mean-velocity derivatives, based on an assumption of local equilibrium.

To accurately resolve the viscous boundary layer of the endwall, a boundary layer grid was created with a thickness that was estimated using the following method. Using a one-seventh power law equation⁸ for turbulent

flow on a flat plate and the experimental boundary layer estimate, which was measured at approximately $0.415C_x$ upstream of the blade leading edge, the distance to the start of the wall from this position was estimated. This distance was added to the length of the grid to estimate the distance from the start of the wall to the exit boundary plane of the grid. Using the lowest Reynolds Number of the various experimental flow conditions the maximum boundary layer thickness of the exit boundary plane of the grid was calculated to be approximately 2.0 inches. The boundary layer grid of the endwall was then constructed using this value.

A boundary layer grid was created for the blade with a thickness of 0.35 inches using the estimated maximum thickness at the blade trailing edge calculated from the same equation used for the endwall.

An initial distance from the wall to the first wall-adjacent centroid, Δy_{init} , of 3.0×10^{-5} inches was chosen to obtain a y^+ on the order of 1 at the boundary layer edge using the formula, $\Delta y_{init} = 10/Re_{C_{x,2}}$, where $Re_{C_{x,2}}$ is from the experimental test condition with the highest value. A tanh boundary layer spacing was used with a 1.1 expansion factor. The cell height outside the boundary layers was also gradually increased using a tanh function.

To perform a grid sensitivity analysis, three grids were constructed starting with 8 million cells and progressively coarsening the grid to 4 and 2 million cells. Grid coarsening was uniform in all directions from one coarsening to the next. Mesh quality decreased, measured by increasing skewness and aspect ratio, as coarsening occurred.

C. Computational Parameters

Computations were performed at the cruise and take-off conditions listed of $+40^\circ$ and -2.5° , respectively. A low turbulence intensity level of 0.325% was used to match experimental estimations⁴. A turbulence length scale of 0.3% of the span was used as calculated by Ameri et al.⁹

III. Experimental Description

The following is a summary of the experimental test that was conducted in the Transonic Turbine Blade Cascade Facility located at NASA Glenn Research Center. Details of the experiment are given in Flegel-McVetta et al.⁴

A. Facility

The Transonic Turbine Blade Cascade Facility is a large scale cascade that allows detailed flow field surveys and blade surface measurements^{10,11,12}. Details of the facility are shown in Fig. 2. The continuous run capability over a large relevant range of Reynolds and Mach numbers along with the ability to vary incidence over a 95° range makes this cascade an ideal first step for testing the VSPT blade design.

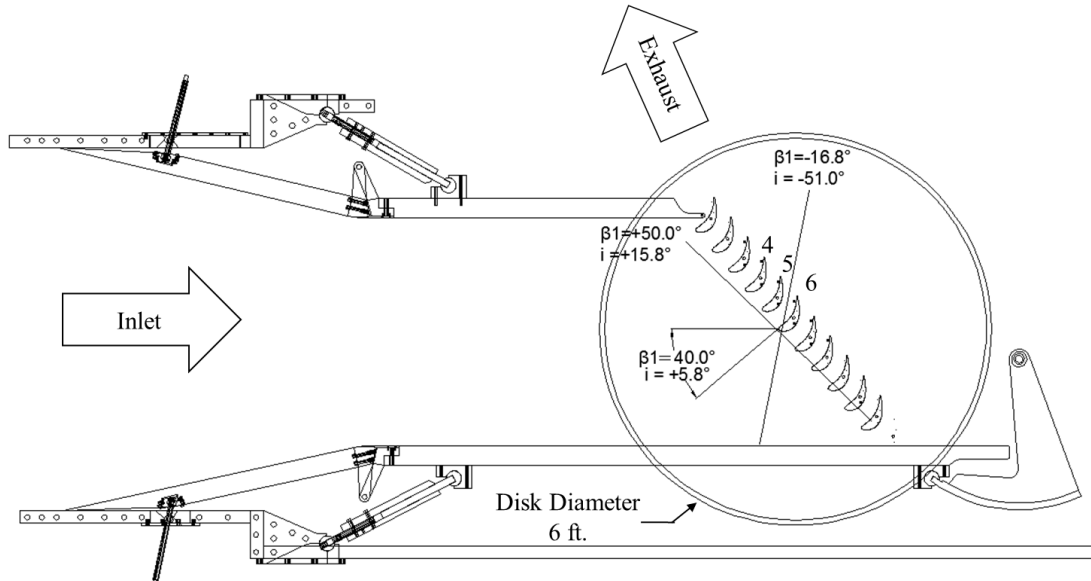


Figure 2. Transonic turbine blade cascade facility.

The cascade was made up of nominally eleven blades. The blade geometry is a scaled 2-D midspan section of a VSPT second stage rotor¹³. Details of the blade geometry are shown in Fig. 3 and described in Table 1. During this

experiment, data were acquired for ten incidence angles spanning $+15.8^\circ \leq i \leq -51.0^\circ$. Two design mission incidence angles which corresponded to take-off ($i = -36.7^\circ$) and cruise ($i = +5.8^\circ$) were the focus for this CFD study. At each incidence angle setting, data were acquired at the five nominal flow conditions. The design pressure ratio was 1.412 which corresponds to an exit isentropic Mach number of 0.72. A baseline flow condition was established by finding the lowest Reynolds number at which the tunnel could consistently maintain an exit Mach number of 0.72. The baseline Reynolds number, Re_b , was found to be 0.53×10^6 . This is the flow condition simulated in this CFD study and is described in Table 2.

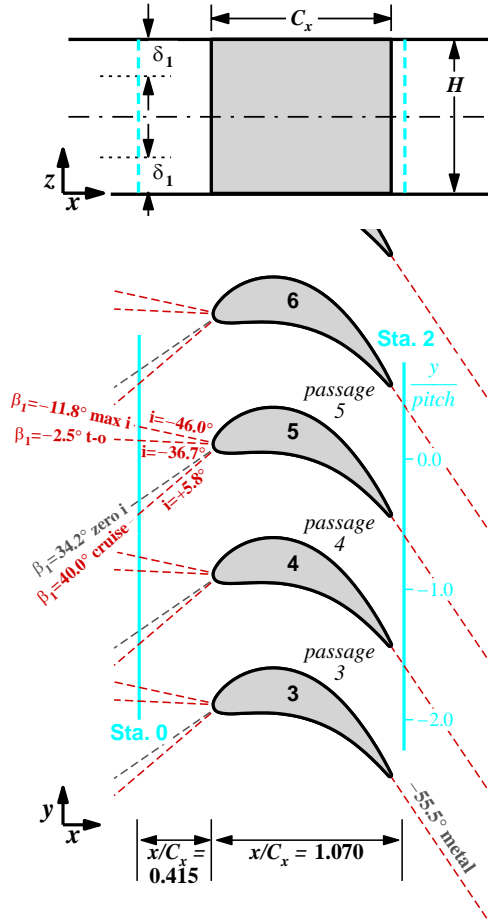


Figure 3. VSPT blade details and measurement station locations.

Table 1. VSPT Blade Description.

Geometry	Value
Axial Chord, C_x	180.57 mm (7.109 inches)
True Chord	194.44 mm (7.655 inches)
Pitch, S	130.00 mm (5.119 inches)
Span, H	152.40 mm (6.000 inches)
Throat Diameter	72.85 mm (2.868 inches)
Leading Edge Diameter	15.16 mm (0.597 inches)
Trailing Edge Diameter	3.30 mm (0.130 inches)
Stagger Angle	20.35°
Inlet Metal Angle	34.2°
Uncovered Turning	19.47°
Exit Metal Angle	-55.54°

Table 2. Angle and Flow Conditions Used in Simulations.

Incidence Angle, i	Inlet Angle, β_1	Inlet Re_{cx}	Exit Re_{cx}	Pressure Ratio	Exit M_{is}	δ_{inlet} in.
-36.7° (Take-off)	-2.5°	294,700	527,400	1.35	0.67	1.50
+5.8° (Cruise)	+40.0°	389,100	531,000	1.41	0.72	1.44

B. Measurement Description

Total-pressure and exit flow angle data were acquired using a five-hole and three-hole pneumatic pressure probe installed 7.0% axial-chord downstream of the blade trailing edge. This survey location is shown as Station 2 in Fig. 3 and traverses across three blade passages. For the $i = -36.7^\circ$ and $i = +5.8^\circ$ incidence angles detailed half-span surveys were acquired over 26 spanwise and 62 pitchwise points. The overall estimated uncertainty in flow angle was $\pm 1.5^\circ$ and the overall estimated uncertainty in total-pressure coefficient was $\pm 0.8\%$ ⁴.

The primary measurement blades 4, 5, and 6 were instrumented with pressure static taps located along 10%, 15%, 30%, and 50% span. Blade 5 was fully instrumented with 44 static taps on the pressure and suction side. To verify periodicity, blade 4 had redundant taps located on the suction-side of the blade where blade 6 had taps located on the pressure-side. The blade static pressures are measured by an electronically scanned pressure system with ± 15 psid modules referenced to atmosphere. A five-point calibration is performed automatically at least once per hour against a high accuracy quartz pressure transducer. The absolute uncertainty of the pressure measurements is believed to be well within ± 0.01 psi.

The inlet turbulence was characterized with a single-wire hotwire anemometer that was installed in the Station 0 survey plane. This study and experiment was run with low inlet turbulence which was documented⁴ as 0.25%-0.40%. Testing at low turbulence will admit transitional flow on the blade surface which is a key challenge of the VSPT application.² Additional studies were conducted at high turbulence intensities (8%-15%) over the wide incidence range. It was found that the extreme positive and negative incidence angles had produced significant differences in the exit flow field due to the higher inlet turbulence and the thinner inlet boundary layer imposed by the turbulence grid¹⁴.

IV. Results and Discussion

As mentioned previously, the main objective of the study was to investigate the computational accuracy of the CFD++ code in terms of blade loading, loss, and turning. The results are compared to experimental data. Results of predicted blade loading, loss, and turning, convergence histories, and different turbulence and transition models are presented in this section.

A. Cruise Angle

1. Steady State Simulations

Steady state numerical computations that use RANS methods were performed to predict the blade loadings for the cruise condition using the k-epsilon turbulence model. Computations were performed on a DOD supercomputer using 96 cores and were carried out until convergence was obtained through monitoring the residual of the energy equation. The convergence history of all residuals of the right hand side of the Navier-Stokes equations is plotted in Fig. 4 against iteration in semi-log format and the solution appears converged by 2000 iterations with all residuals having dropped at least four orders of magnitude.

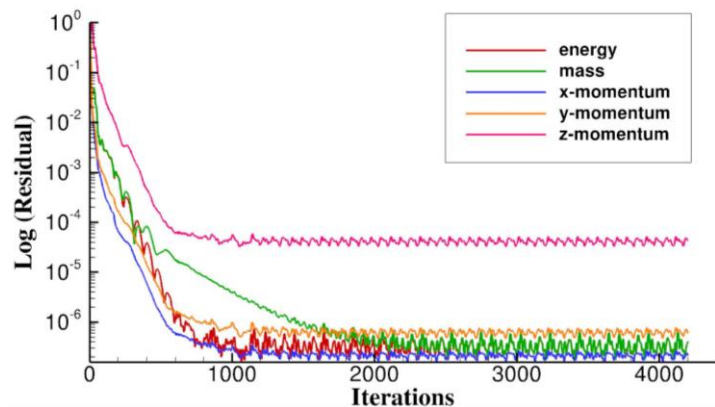


Figure 4. Residual convergence plot for cruise condition steady state simulation.

2. Turbulence and Transition Model Comparisons.

RANS solutions were obtained using the k-epsilon turbulence model, with and without use of the algebraic transition model I, and the Langtry-Menter model. The algebraic transition model I modifies the term responsible for the rate of production of turbulence energy in the transport equations for k and epsilon. The modification is based on a correlation using the parameter, $\frac{k\Omega}{vS^2}$, where k is turbulence kinetic energy, Ω is mean vorticity magnitude, ν is molecular kinematic viscosity, and S is mean strain magnitude⁶. For comparison purposes RANS solutions were also obtained for the SST model with and without use of the algebraic transition model II. Fig. 5 compares the solutions to the experimental blade surface pressure midspan data for the cruise condition. As can be seen with the k-epsilon turbulence model, the use of the transition model captures a pressure drop present in the experimental data on the suction side at x/C_x from 0.7 to 0.9 and thus predicts the separation/reattachment in this region suggested by the experimental data. This flow feature does not appear in results without the transition model. Agreement with the experimental data is generally good for other locations of the suction side for both results with and without use of the transition model, however the results slightly over predict pressures close to the leading edge and under predict it starting at approximately $x/C_x = 0.4$ and continuing to the trailing edge. For the pressure side, agreement of results with experiment is also generally good with and without use of the algebraic transition model I.

As can be seen from Fig. 5, the Langtry-Menter turbulence/transition model performed similarly to the k-epsilon turbulence/algebraic transition model I on the suction side however it predicted the pressure drop near the trailing edge with too quick of a recovery at $x/C_x = 0.8$. For the pressure side, the Langtry-Menter model slightly under predicted pressures. RANS solutions for the pressure distribution were obtained for the two-equation SST model with the algebraic transition model II, however results compared poorly to experiment and are not presented.

A comparison of skin friction predictions on the suction surface at midspan was made for all models and is shown in Fig 6. As can be seen with the SST turbulence model transition occurred abruptly close to the leading edge. The SST turbulence model with the algebraic transition model II shows a long transition completing at approximately $x/C_x = 0.95$. The Langtry-Menter model shows a transition occurring at approximately $x/C_x = 0.90$. The k-epsilon turbulence model with the algebraic transition model I shows transition occurring in the same approximate location as Langtry-Menter model. All three transition models appear to show separation occurring prior to the transition. For further comparison purposes a solution was obtained with the k-epsilon turbulence model using a simulated trip wire placed at $x/C_x = 0.45$, and a very low

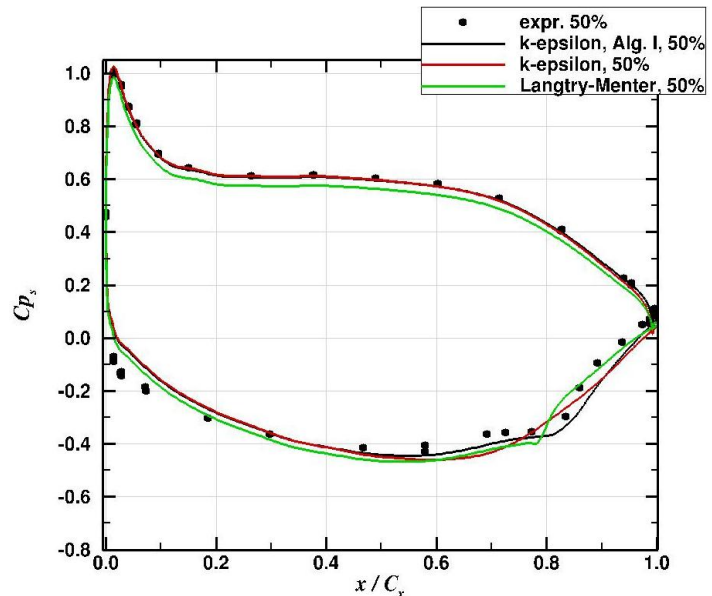


Figure 5. Turbulence and transition model comparison for cruise condition midspan pressure distributions.

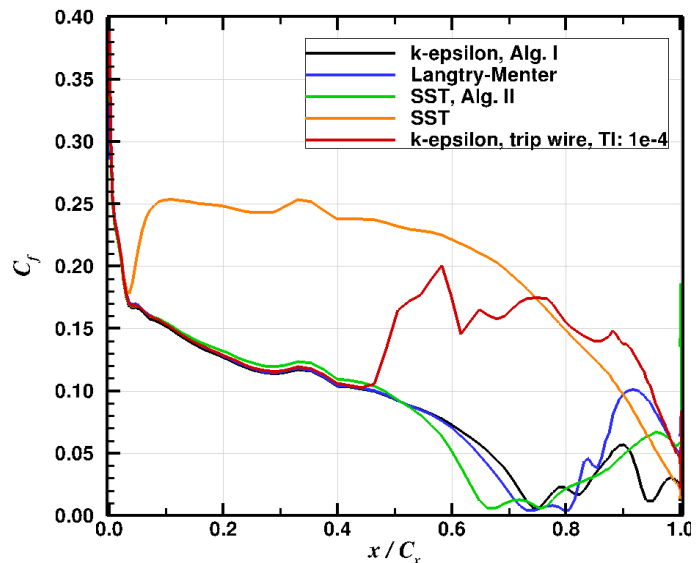


Figure 6. Comparison of skin friction predictions of several turbulence and transition models.

turbulence intensity of $1e-4$ to keep the flow laminar prior to tripping, and transition can be seen to occur at that location.

Comparisons of other turbulence and transition models included in the CFD++ code could not be performed as they did not work with the Musker inflow velocity profile boundary condition. No experimental data was available to compare the skin friction predictions to. Overall, as the k-epsilon turbulence model with the algebraic transition model I matched best to experiment for pressure distribution it was used for the remainder of this study.

3. Unsteady Time Accurate Simulations

Unsteady time accurate simulations were performed to observe any differences in the results from the RANS simulations. The URANS model used the k-epsilon turbulence model with algebraic transition model I.

As the fundamental frequency of unsteadiness was unknown the correct time step to use was also unknown. The time of flight of flow through the grid was calculated to be 0.004 seconds. This value was used as a gauge for estimating a correct time step and several solutions were obtained at time steps ranging from $1e-3$ to $4e-5$ seconds. These time step ranges represent a range from 4 iterations per time of flight to 100 iterations per time of flight.

After convergence was obtained, the solutions were time averaged, varying the averaging process from 0.5 up to a maximum of a 1 second time period to ensure that a long time average was conducted to average over many periods (ensembles) of unsteadiness.

Some of the results are presented in Fig. 7 and as can be seen from the plots there was almost no difference between results for predicted pressure distribution for RANS and URANS calculations. In addition, there were almost no differences between URANS computations performed using different time steps or computations averaged over different iteration amounts using the same given time step. Therefore RANS simulations appeared to perform adequately for predicting midspan pressure distributions for the cruise condition.

4. Grid Sensitivity Study

A study was performed to observe sensitivity of accuracy of results to change from 8 million to 2 million grid points in the resolution of fluid flow scales in the chordwise, spanwise, and pitchwise directions. A comparison plot for the midspan pressure distribution is shown in Fig. 8 and it can be seen that results are consistent for the 8 and 4 million point grids. The 2 million point grid showed significant differences in results compared to the other resolutions. Comparisons for the different grid densities were made using results for the cruise condition area averaged Cp_i versus z/H at 0.07 axial chord downstream and total pressure loss for the midspan location at 0.07 axial chord downstream. Plots for these results are presented later in the paper in Fig. 12 and 13, respectively. Again, results were consistent for the 8 and 4 million point grids. The solutions for the 2 million point grid again

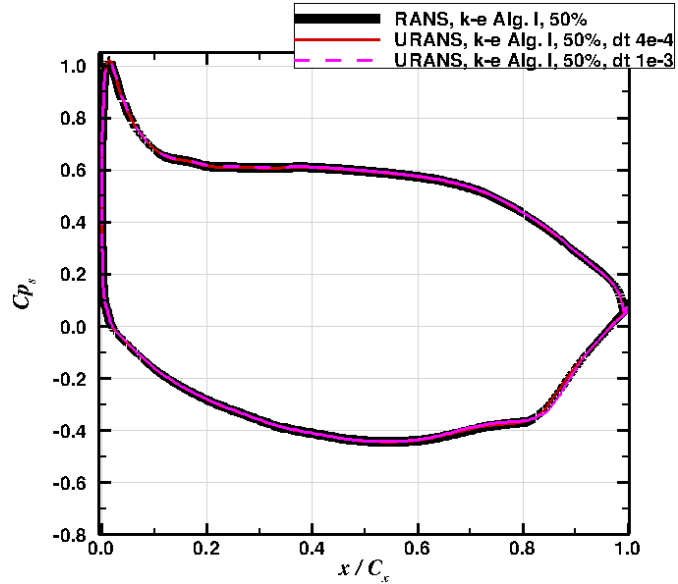


Figure 7. Unsteady time accurate simulation comparisons.

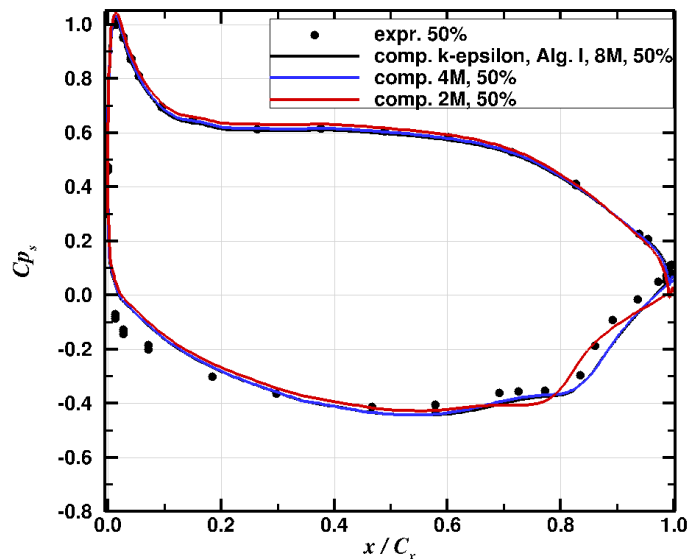


Figure 8. Comparison of grid resolution for cruise condition midspan pressure distribution predictions.

showed significant differences in results and are not presented in these figures.

It was demonstrated that solution results were independent of grid refinement at 4 million points, with the 4 and 8 million point grids producing similar results. All further results presented in this paper were obtained using the 8 million point grid.

5. Pressure Distribution

Comparisons of RANS computational results to experimental measurements for the blade pressure distributions were made. Fig. 9 compares solutions to experiment for blade surface pressures for the cruise condition at four spanwise locations. Experimental results were measured on three blades but the legend is consolidated in this paper. Overall good agreement is observed between the computations and experimental data. At $x/C_x = 0.7 - 0.9$ the computations predict the suction side separation/reattachment at mid span suggested by the experimental data (black circles). Pressure side agreement with the data is excellent. At other span locations, which are inside the boundary layer of the endwall, the computations as shown in Fig. 9 also appear to agree well with the data. Although there are few experimental data on the suction side near the trailing edge at these spanwise locations the computations go through the data points.

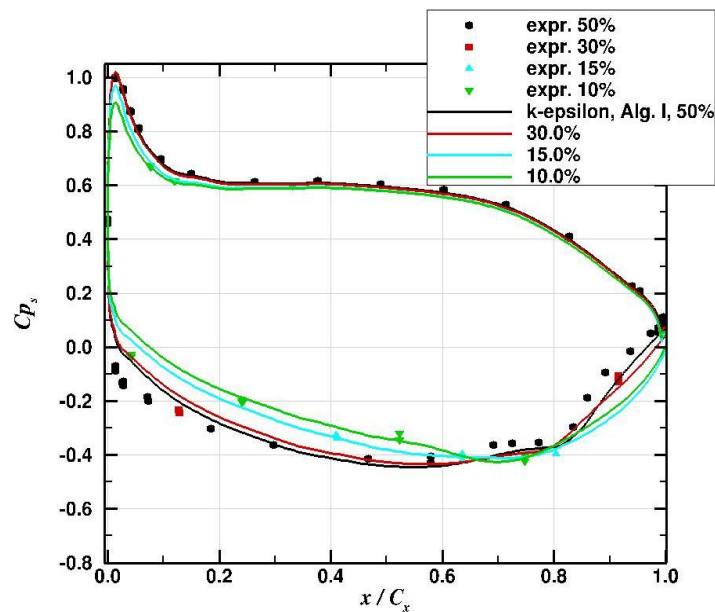
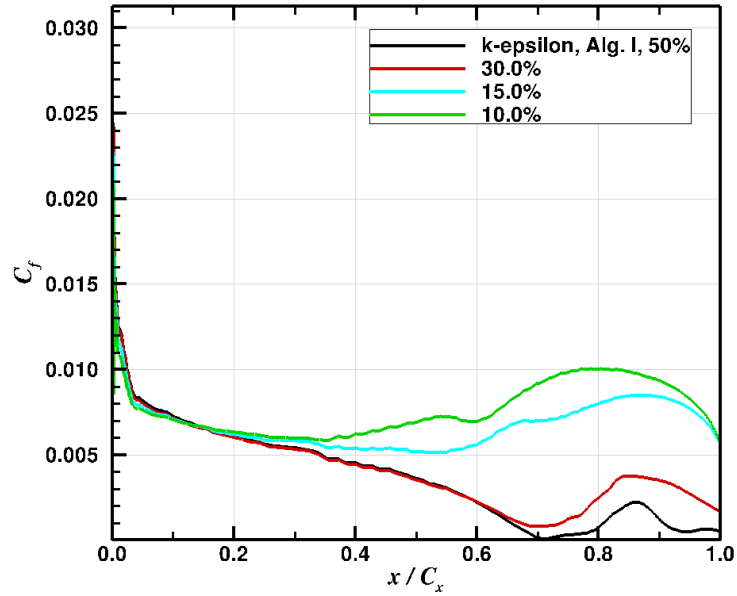


Figure 9. Comparison of RANS k-epsilon turbulence model with algebraic transition model I to experiment for cruise condition pressure distributions at four spanwise locations.

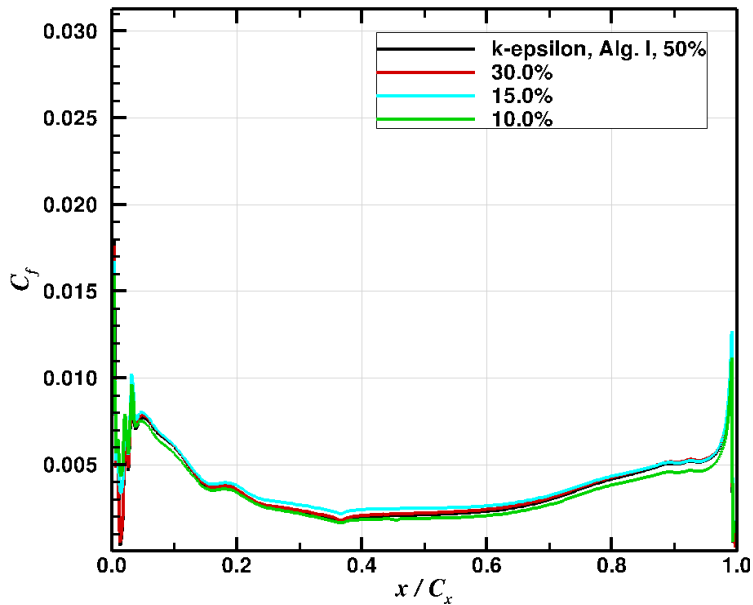
6. Skin friction Plots

As shown in Fig. 10 (a) the solution shows laminar flow on the suction side leading to separation at an axial location of 70% at midspan. The computation suggests that a separation bubble reattaches at around 80%. It may separate again at 95% axial chord without closing. The area of separation predicted by the code near the axial location of 80% matches the inflection in the experimental pressure distribution, which suggests that the boundary layer did actually separate. The agreement with the data is indicative of the correctness of the prediction provided by the solution for this case. In Fig. 10 (b) the pressure side appears to show a long transition before the flow becomes turbulent.

In the spanwise direction transition occurs earlier on the suction side approaching the endwall. Transition is very three dimensional and seems to be triggered along the pressure side leg of the measured horseshoe vortex running up on the suction side⁴. Transition appeared fairly consistent in the spanwise direction for the pressure side.



(a)



(b)

Figure 10. Skin friction plots for cruise condition at four spanwise locations; (a) suction side and (b) pressure side.

7. Exit Total Pressure

Comparisons of computational results to experimental measurements for the blade wake region were made. Fig. 11 compares plots of C_{p_t} contours at 7 percent axial chord downstream of the trailing edge, with Fig. 11 (a) showing measured contours⁴ and Fig. 11 (b) showing the computed contours. The match in location is good, although the thickness of the wake is narrower. Agreement of results is good for the loss core due to the pressure side leg of the horseshoe vortex, corresponding to the experimental data at (-0.55, 0.38). Results over predict the loss core in the region of the wake of the blade, corresponding to the region (-0.55, 0.5) due to the separated flow in the vicinity of midspan. The results under predict the third loss core close to the hub due to the wake and endwall boundary layer interaction corresponding to the region near (-0.5, 0.02).

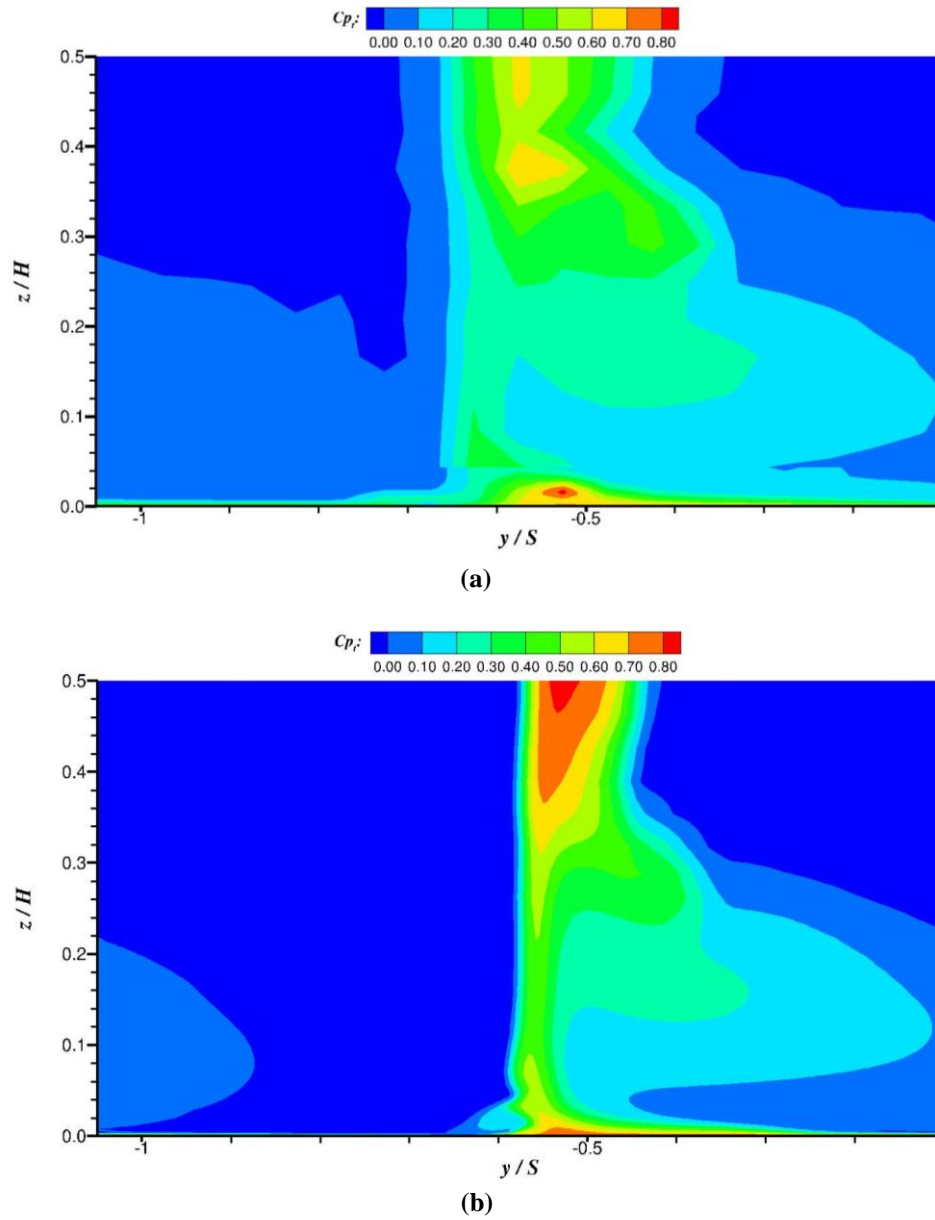


Figure 11. C_{p_t} contours for cruise condition at 0.07 axial chord downstream of the trailing edge; (a) data from (Ref. 4) and (b) computed.

Fig. 12 compares plots of computed and measured midspan total pressure loss at 7 percent axial chord downstream. The computations predict a narrower wake but over predict the maximum C_{p_t} value, and locate it slightly higher in the pitchwise direction. In addition computed values of C_{p_t} outside the wake are negative in value, which may be caused by numerical inaccuracy in the code.

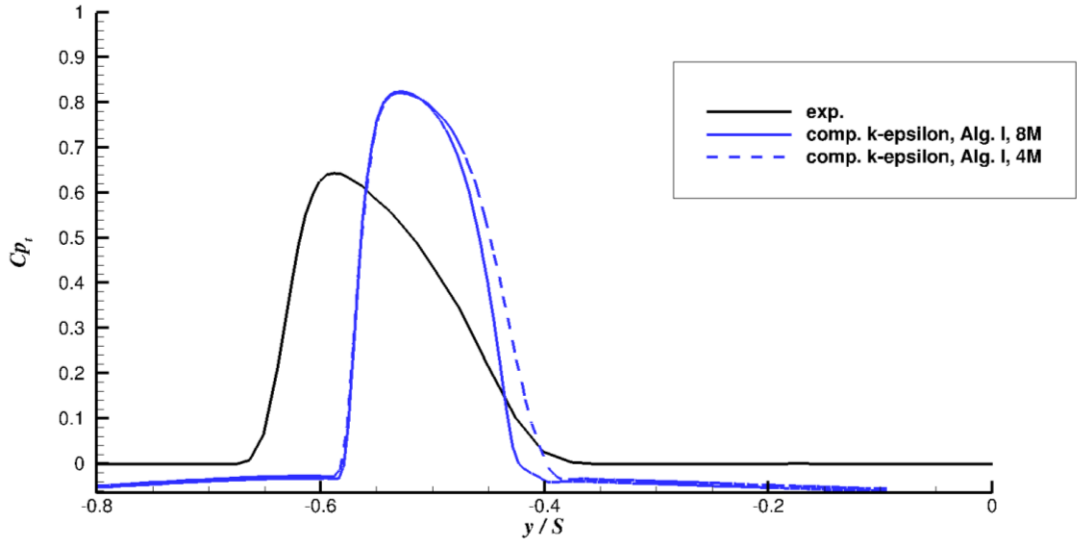


Figure 12. Cruise condition total pressure loss 0.07 axial chord downstream of midspan location.

Fig. 13 shows a comparison of computational and experimental area averaged total pressure coefficient versus the span wise direction for the cruise condition. Experimental measurements are shown for two adjacent passages (to verify periodicity)⁴ and comparison shows that the computational results mostly under predicted total pressure coefficient with agreement being very good up to $z/H = 0.2$ and the greatest difference occurring at approximately $z/H = 0.38$. This difference is likely due to the thinner wake predicted at that location for the loss core due to the pressure side leg of the horseshoe vortex.

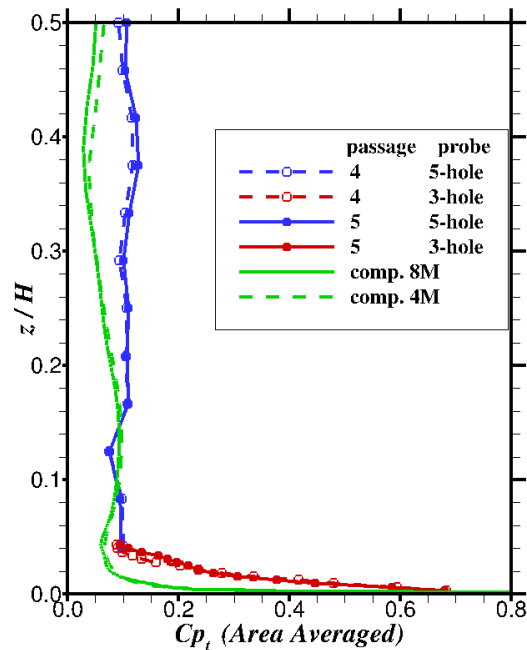


Figure 13. Area averaged losses versus z/H at 0.07 axial chord downstream for cruise condition.

8. Exit Angle Comparison

Fig. 14 shows a plot comparing experimental pitchwise mass-averaged exit flow angle, β , to the computed angle for the cruise condition. Agreement between experiments and computation is very good from $z/H = 0.1 - 0.3$ and then diminishes toward midspan. From $z/H = 0.1 - 0.0$, approaching the highly overturned region very near the endwall, agreement also diminishes.

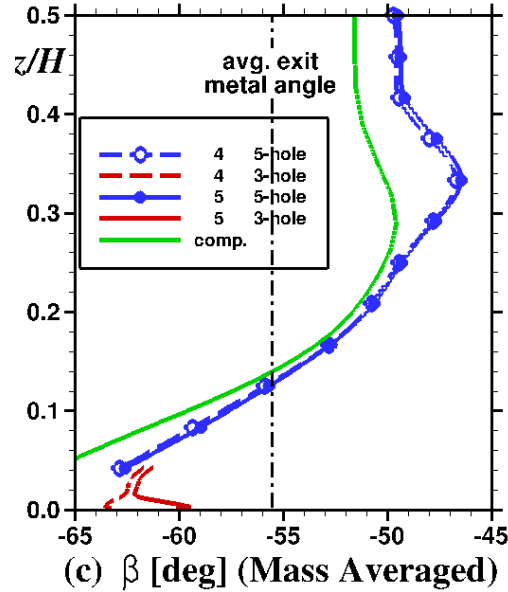


Figure 14. Mass averaged pitchwise exit angle at 0.07 axial chord downstream for cruise condition.

B. Take-off Angle

1. Unsteady Time Accurate Simulations

Significant differences between RANS and URANS calculations suggested that the flow is unsteady. The URANS solutions obtained were more accurate and the results are presented here. Convergence criteria, time step and averaging were chosen similar to as for the cruise condition.

2. Pressure Distribution

Comparisons of URANS computational results to experimental measurements for the take-off condition blade pressure distributions were made.

Fig. 15 compares computations to experiment for static pressure coefficient at four spanwise locations. The highly negative incidence (-36.7°) produces an inverted pressure distribution in the leading edge region of the blade with the loading reverting to nominal beyond 20 percent x/C_x from the leading edge.⁹ The plots show good agreement between computations and experiment. On the pressure side computations reveal regions of separation across the span near the leading edge until $x/C_x = 0.25$ although there are not enough experimental data points to confirm if this is the case. Good agreement with the data is shown for the suction side. A slight plateau in the experimental data starting at $x/C_x = 0.7$

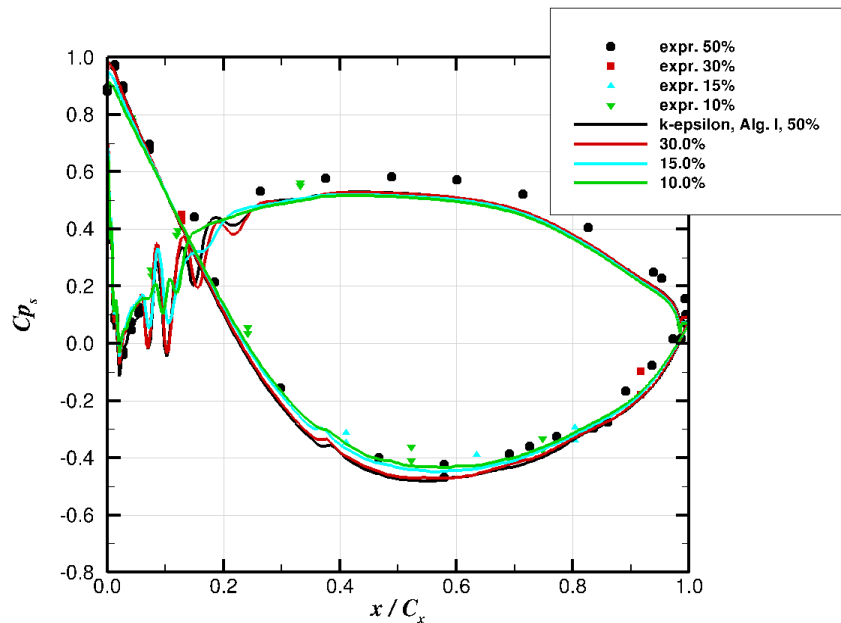


Figure 15. Comparison of URANS computations to experiment for take-off condition pressure distributions at four spanwise locations.

suggesting possible separation is partially represented in the computational results.

3. Skin friction

As shown in Fig. 16 (a) for the suction side early transition is predicted at an axial location of 35%. There is reduced three dimensionality for transition location compared to the cruise condition which is consistent with expectations as the blade is lightly loaded at the take-off condition. The pressure side plots, as shown in Fig. 16 (b), suggest the presence of separation in the region close to the leading edge with transition to turbulent flow. There is small spanwise variation in transition location observed in the results.

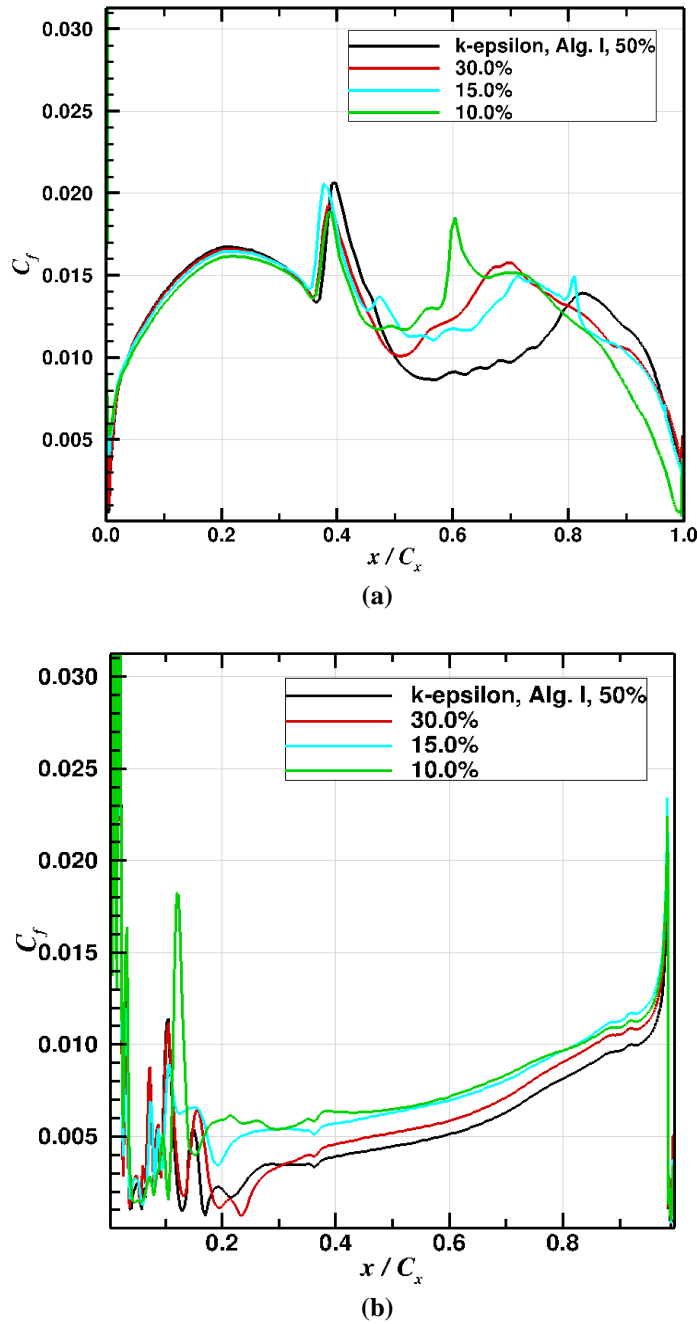


Figure 16. Skin friction plots for take-off condition at four spanwise locations; (a) suction side and (b) pressure side.

4. Exit Total Pressure

Fig. 17 compares experimental and computed plots of C_{p_t} contours at 0.07 axial chord downstream of the trailing edge. As a result of the unloading of the blade, the secondary flow system in the passage weakens and there is a reduced variation in pressure loading in the spanwise location.⁹ This causes the contours to differ from the cruise condition. As seen in Fig. 17(a), the pressure side leg of the horseshoe vortex is present in the lower portion of the blade span at (-0.5, 0.14) due to the weakening of the passage vortex. The endwall wake interaction is still present in the same location as for the cruise condition (-0.5, 0.02). As seen in Fig. 17(b), computed results qualitatively match very closely with the measurements with these features located in the same regions. Overall computed total pressure coefficients were predicted slightly higher than experimental values.

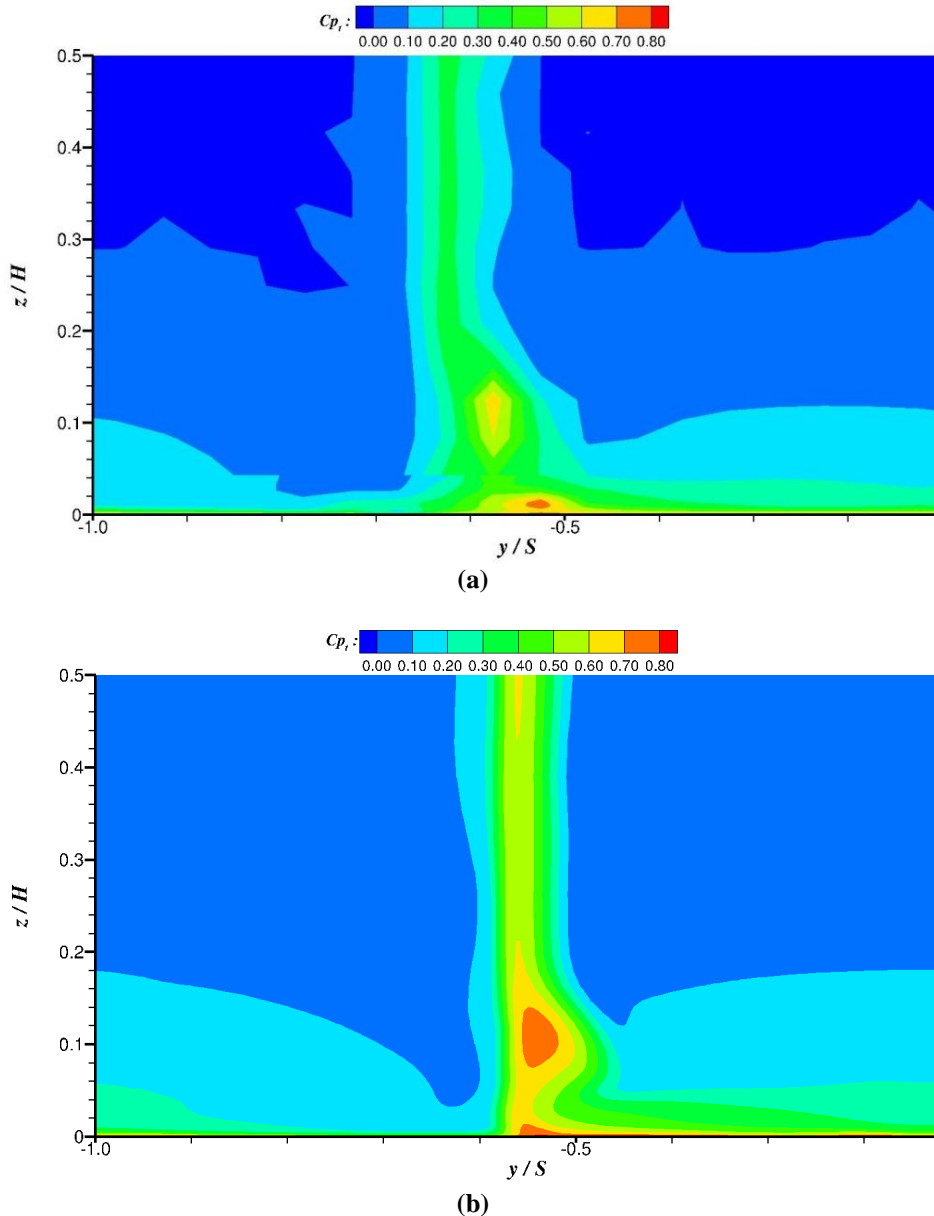


Figure 17. C_{p_t} contours for take-off condition at 0.07 axial chord downstream of the trailing edge; (a) data from (Ref. 4) and (b) computed.

Fig. 18 compares computational and experimental plots of total pressure loss 0.07 axial chord downstream for the midspan location. As can be seen in Fig. 18 computations over predict the maximum C_{p_t} value and there is some misalignment in the computed pitchwise location of the wake compared to measurements. These differences appear consistent with the differences in magnitude and location of the wake at midspan seen between Fig. 17(a) and (b).

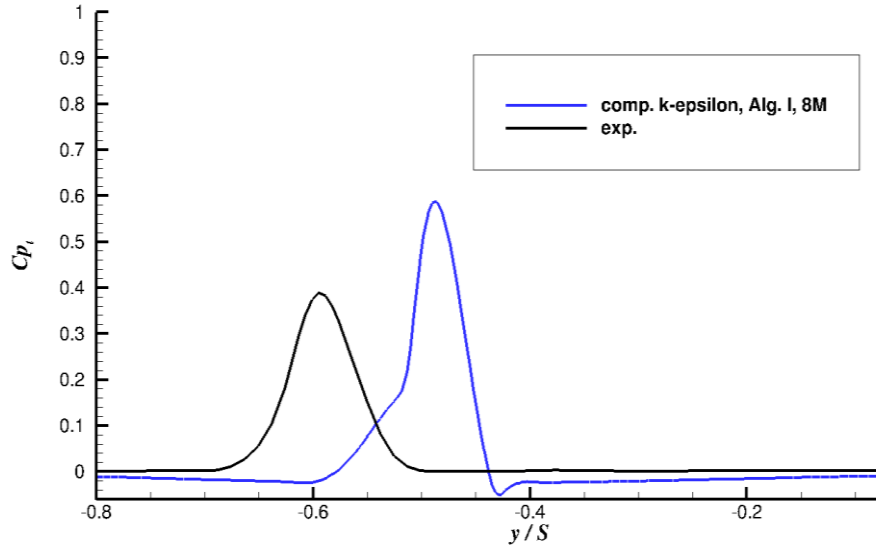


Figure 18. Take-off condition total pressure loss 0.07 axial chord downstream for midspan location.

Fig. 19 compares computational and experimental plots of pitchwise area averaged total pressure coefficient at the 0.07 axial chord position downstream of the blade. Experimental measurements are shown for two adjacent passages 4 and 5 to verify periodicity⁴. Comparison of computational results to experiments is fair showing a qualitative similarity however the computational results consistently over predicted total pressure coefficient throughout the length of the plot away from the endwall region.

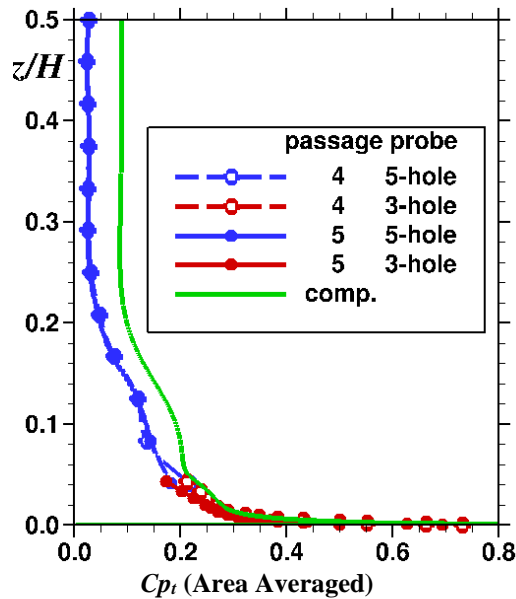


Figure 19. Area averaged losses versus z/H at 0.07 axial chord downstream for take-off condition.

5. Exit Angle Comparison

Fig. 20 shows a comparison plot of experimental pitchwise mass-averaged exit flow angle, β , to the computed angles for the take-off condition. Agreement between experiments and computations is very good with differences being no more than 2° except from $z/H = 0.02 - 0.08$ where differences are approximately 2.5° , which is slightly outside the uncertainty range of the experiments.

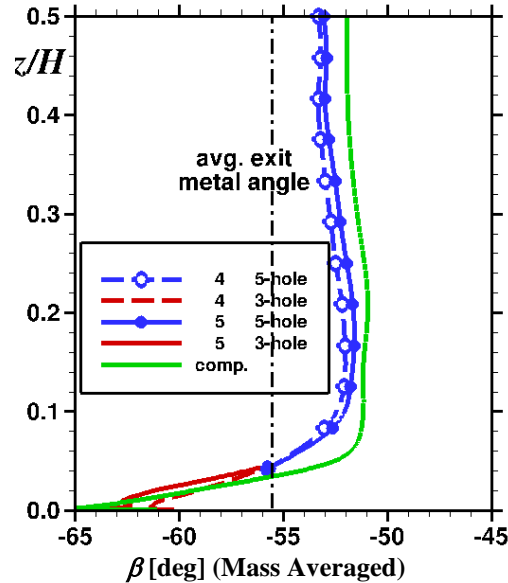


Figure 20. Mass averaged pitchwise exit angle at 0.07 axial chord downstream for take-off condition.

V. Conclusions

The VSPT blade operates over a wide range of incidence angles. The design/cruise condition of the VSPT blade represents a highly loaded condition with transitional flow on the blade, while the take-off condition represents an extreme off-design operating condition where the blade row is unloaded.

Evaluation of the predictive performance of a COTS software code, CFD++, was performed using experimental data provided by Flegel-McVetta *et al.*, 2013⁴, of a VSPT blade midspan section tested in a transonic linear cascade. CFD computations were obtained at two blade incidence angle conditions corresponding to the turbine cruise design point condition and the take-off design point condition. The CFD code was assessed in terms of blade loading, loss, and turning against test data from the transonic tunnel.

Computations of the three dimensional blade loadings agreed with the data for both conditions and were able to capture laminar separation on the aft 30% of the suction side for the cruise condition. Pressure side separation near the leading edge was predicted for the take-off condition, although this was not confirmed due to a lack of data.

For the total pressure survey downstream of the blade, agreement with the data was very good close to the end-wall and diminished toward midspan. For the cruise condition computational results under predicted total pressure coefficient while for the take-off incidence the results over predicted it.

Agreement for the exit flow angle measurements was fair for the cruise angle and was mostly within about 2.5 degrees, which is slightly outside the uncertainty range of the experiments, except for the region at $z/H = 0.34$ where it diminished further. Agreement for the take-off angle was good with differences being no more than 2° except for the region at $z/H = 0.06$ where differences approached approximately 2.5°.

Overall the CFD++ code and grid technique showed fair to good results compared to experiment for the VSPT blade. The combined k-epsilon turbulence model and algebraic transition model I produced the closest overall agreement with experiment, although further model comparisons should be made in the future as the code develops more capability. Further assessment should be done to improve the understanding of the capability of turbulence and transition codes and to improve predictions. In addition comparisons at other Reynolds numbers should be made to understand sensitivity of results to Reynolds number changes.

References

- ¹ D'Angelo, M., "Wide Speed Range Turboshaft Study," NASA CR-198380, August 1995.
- ² Welch, G.E., 2010, "Assessment of Aerodynamic Challenges of a Variable-Speed Power Turbine for Large Civil Tilt-Rotor Application," Proc. AHS Int. 66th Annual Forum, May; also NASA TM-2010-216758, Aug.
- ³ Welch, G.E., Giel, P.W., Ameri, A.A., To, W., Skoch, G.J., Thurman, D.R., "Variable-Speed Power-Turbine Research at Glenn Research Center," Proc. AHS Int. 68th Annual Forum, May; also NASA TM-2012-217605, July.

⁴ Flegel-McVetta, A.B, Giel, P.W., Welch, G.E., “Aerodynamic Measurements of a Variable-Speed Power-Turbine Blade Section in a Transonic Turbine Cascade at Low Inlet Turbulence,” NASA TM-2013-218069, April.

⁵ CFD++, Metacomp Technologies, Inc., Agoura Hills, CA.

⁶ CFD++ and CAA++ User Manual, Version 11.1, Metacomp Technologies, Inc., Agoura Hills, CA.

⁷ Pointwise, Pointwise, Inc., Fort Worth, TX.

⁸White, F. M., *Viscous Fluid Flow*, 3rd ed., McGraw Hill, New York, 2006, Chap. 6.

⁹ Ameri, A., Giel, P. W., McVetta, A. B., “Validation of a CFD Methodology for Variable Speed Power Turbine Relevant Conditions,” ASME GT2013-95030, Jun, 2013; also NASA TM-2013-217860, May.

¹⁰ Verhoff, V. G., Camperchioli, W. P, and Lopez, I., 1992, “Transonic Turbine Blade Cascade Testing Facility”, AIAA Paper No. 92-4034; also NASA TM-105646, Nov. 1995.

¹¹ Giel, P.W., Sirbaugh, J.R, Lopez, I., and Van Fossen, G. J., “Three Dimensional Navier-Stokes Analysis and Redesign of an Imbedded Bellmouth Nozzle in a Turbine Cascade Inlet Section,” ASME *Journal of Turbomachinery*, 118, No 3, 1996, pp 529-535; also NASA TM-107284, Oct. 1996 and U.S. Army ARL-MR-152, July 1996.

¹² McVetta, A. B., Giel, P. W., and Welch, G. E., “Aerodynamic Investigation of Incidence Angle Effects in a Large Scale Transonic Turbine Cascade,” AIAA-2012-3879, *Proc. 48th AIAA/ASME/SAE/ASEE Joint Propulsion Conference & Exhibit*, Atlanta, GA, Jul-Aug. 2012.

¹³ Ford, A, Bloxham, M., Turner, E., Clemens, E. and Gegg, S., “Design Optimization of Incidence-Tolerant Blading Relevant to Large Civil Tilt-Rotor Power Turbine Applications,” NASA CR-2012-217016, Dec. 2012.

¹⁴ Flegel, A.B., Giel, P.W., Welch, G.E., “Aerodynamic Effects of High Turbulence Intensity on a Variable-Speed Power-Turbine Blade with Large Incidence and Reynolds Number Variations,” AIAA-2014-3933, *Proc. 50th AIAA/ASME/SAE/ASEE Joint Propulsion Conference & Exhibit*, Cleveland, OH, July 2014.